The Astrophysical Journal, 779:163 (9pp), 2013 December 20 doi:10.1088/0004-637X/779/2/163

NuSTAR OBSERVATIONS OF MAGNETAR 1E 1841−045

Hongjun An[1], Romain Hascoët[2], Victoria M. Kaspi[1,13], Andrei M. Beloborodov[2], François Dufour[1], Eric V. Gotthelf[2], Robert Archibald[1], Matteo Bachetti[3,4], Steven E. Boggs[5], Finn E. Christensen[6], William W. Craig[5,7], Brian W. Greffenstette[8], Charles J. Hailey[2], Fiona A. Harrison[8], Takao Kitaguchi[9], Chryssa Kouveliotou[10], Kristin K. Madsen[8], Craig B. Markwardt[11], Daniel Stern[12], Julia K. Vogel[7], and William W. Zhang[11]

[1] Department of Physics, McGill University, Montreal, Quebec H3A 2T8, Canada
[2] Columbia Astrophysics Laboratory, Columbia University, New York, NY 10027, USA
[3] Université de Toulouse, UPS-OMP, IRAP, Toulouse, France
[4] CNRS, Institut de Recherche en Astrophysique et Planétologie, 9 Av. colonel Roche, BP 44346, F-31028 Toulouse Cedex 4, France
[5] Space Sciences Laboratory, University of California, Berkeley, CA 94720, USA
[6] DTU Space, National Space Institute, Technical University of Denmark, Elektrovej 327, DK-2800 Lyngby, Denmark
[7] Lawrence Livermore National Laboratory, Livermore, CA 94550, USA
[8] Cahill Center for Astronomy and Astrophysics, California Institute of Technology, Pasadena, CA 91125, USA
[9] RIKEN, 2-1 Hirosawa, Wako, Saitama 351-0198, Japan
[10] Space Science Office, ZP12, NASA Marshall Space Flight Center, Huntsville, AL 35812, USA
[11] Goddard Space Flight Center, Greenbelt, MD 20771, USA
[12] Jet Propulsion Laboratory, California Institute of Technology, Pasadena, CA 91109, USA
Received 2013 August 12; accepted 2013 October 22; published 2013 December 3

ABSTRACT

We report new spectral and temporal observations of the magnetar 1E 1841−045 in the Kes 73 supernova remnant obtained with the *Nuclear Spectroscopic Telescope Array*. Combined with new *Swift* and archival *XMM-Newton* and *Chandra* observations, the phase-averaged spectrum is well characterized by a blackbody plus double power law, in agreement with previous multimission X-ray results. However, we are unable to reproduce the spectral results reported based on *Suzaku* observations. The pulsed fraction of the source is found to increase with photon energy. The measured rms pulsed fractions are ∼12% and ∼17% at ∼20 and ∼50 keV, respectively. We detect a new feature in the 24–35 keV band pulse profile that is uniquely double peaked. This feature may be associated with a possible absorption or emission feature in the phase-resolved spectrum. We fit the X-ray data using the recently developed electron–positron outflow model by Beloborodov for the hard X-ray emission from magnetars. This produces a satisfactory fit, allowing a constraint on the angle between the rotation and magnetic axes of the neutron star of ∼20° and on the angle between the rotation axis and line of sight of ∼50°. In this model, the soft X-ray component is inconsistent with a single blackbody; adding a second blackbody or a power-law component fits the data. The two-blackbody interpretation suggests a hot spot of temperature $kT \approx 0.9$ keV occupying ∼1% of the stellar surface.

Key words: pulsars: individual (1E 1841−045) – stars: magnetars – stars: neutron

Online-only material: color figures

1. INTRODUCTION

Magnetars are isolated neutron stars whose X-ray luminosities are thought to be powered by the decay of their intense magnetic fields (Duncan & Thompson 1992; Thompson & Duncan 1996). They are observed as pulsating X-ray sources that occasionally produce bright bursts on timescales as short as 10 ms, as well as major enhancements in the persistent emission lasting days to months (for reviews, see Woods & Thompson 2006; Mereghetti 2008; Rea & Esposito 2011). Magnetic fields inferred from magnetar spin-down rates in many cases exceed 10^{14} G (e.g., 1E 1841−045, SGR 1806−20; Vasisht & Gotthelf 1997; Kouveliotou et al. 1998), although weaker fields are suggested by recent observations of several magnetars (e.g., SGR 0418+5729, Swift J1822.3−1606; Rea et al. 2010, 2012; Livingstone et al. 2011; Scholz et al. 2012). There are 26 magnetars that have been discovered to date, including candidates (see Olausen & Kaspi 2013).[14]

The X-ray spectra of magnetars often require two or more components. The soft X-ray component (which has a peak at ∼1 keV) is thought to be dominated by surface emission from the neutron star and is likely modified by resonant scattering in the magnetosphere (Thompson et al. 2002). It can be fitted by an absorbed blackbody plus a power law or sometimes by a two-blackbody model. The hard X-ray component (which peaks in a νF_ν spectral representation above 100 keV; Kuiper et al. 2006; Enoto et al. 2010) is believed to be generated in the magnetosphere. Its origin has been discussed by several authors (Thompson & Beloborodov 2005; Heyl & Hernquist 2005; Baring & Harding 2007; Beloborodov & Thompson 2007). Recently, Beloborodov (2013) proposed a detailed model of hard X-ray emission from the relativistic outflow created by $e^\pm$ discharge near the neutron star.

The Galactic magnetar 1E 1841−045 is located at the center of the shell-type X-ray and radio supernova remnant (SNR) Kes 73 and was first identified as an anomalous X-ray pulsar by Vasisht & Gotthelf (1997). Its slow 11.8 s spin period and rapid spin-down rate imply an extreme magnetic field of $B \equiv 3.2 \times 10^{19}(P\dot{P})^{1/2}$ G $= 6.9 \times 10^{14}$ G, assuming the dipole spin-down model. Hard X-ray emission was detected by Molkov et al. (2004) and reported by Kuiper et al. (2004, 2006)

[13] Lorne Trottier Chair; Canada Research Chair.
[14] See the McGill SGR/AXP Online Catalog for a compilation of known magnetar properties: http://www.physics.mcgill.ca/~pulsar/magnetar/main.html.

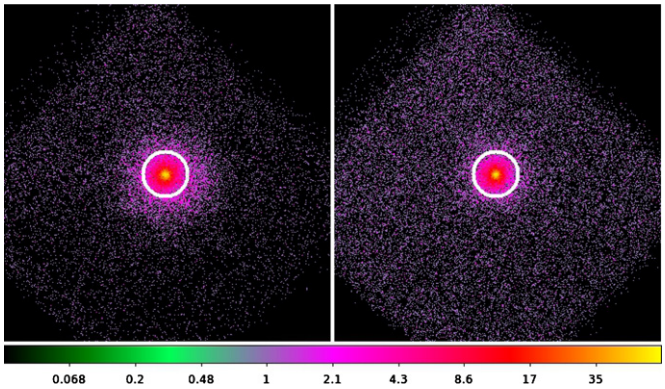

Figure 1. *NuSTAR* images of 1E 1841−045 in the 3–7 keV (left) and 7–79 keV (right) bands in logarithmic scale. Circles of 1′ radius are shown in white. Energy bands were chosen such that the two images have similar number of events in the 1′ circle; the scale beneath the plots shows the number of events per pixel. Note that the diffuse Kes 73 emission ($R \sim 2'$) is visible in the low-energy image but not in the high-energy one.

(A color version of this figure is available in the online journal.)

to be highly pulsed, approaching 100% from 15 to 200 keV. Spectral studies by these authors measured a hard power-law photon index of ∼1.3 in the ∼20–300 keV band using the *Rossi X-Ray Timing Explorer* (*RXTE*) and *International Gamma-Ray Astrophysics Laboratory* (*INTEGRAL*). However, Morii et al. (2010) modeled the spectrum obtained with *Suzaku* with an absorbed blackbody plus two power laws and found results only marginally consistent with those of Kuiper et al. (2006).

In this paper, we report on the spectral and temporal properties of 1E 1841−045 in the 0.5–79 keV band, measured with the *Nuclear Spectroscopic Telescope Array* (*NuSTAR*), the *Swift* X-Ray Telescope (XRT), *XMM-Newton*, and *Chandra*. In Section 2, we describe the observations used in this paper, and in Section 3 we present the results of our data analysis. In Section 3.4, we apply the model of Beloborodov (2013) to our measurements of the hard X-ray emission from 1E 1841−045. We show that our spectral fitting yields results consistent with the expectations from the Beloborodov model. Section 4 presents our discussion and conclusions. These are summarized in Section 5.

2. OBSERVATIONS

NuSTAR is the first satellite mission to have focusing capability above ∼10 keV (Harrison et al. 2013). It is composed of two sets of focusing optics (Hailey et al. 2010) and two CdZnTe focal-plane modules (Harrison et al. 2010; each focal-plane module has four detectors). The observatory operates in the 3–79 keV band with FWHM energy resolution of 400 eV at 10 keV, angular resolution of 58″ (half-power diameter; 18″ FWHM), and temporal resolution of 2 μs (see Harrison et al. 2013 for more details).

We began observing 1E 1841−045 with *NuSTAR* on 2012 November 9 at UT 22:00:02.184, with a total net exposure of 48.6 ks. Although *NuSTAR* is extremely sensitive in the hard X-ray band, a simultaneous 18 ks *Swift* XRT observation (photon-counting mode) was conducted at UT 21:49:38.742 on 2012 November 9 to extend the spectral coverage down to ∼0.5 keV, where the thermal component is dominant.

The *NuSTAR* data were processed with `nupipeline` 1.1.1 along with CALDB version 20130509, and the *Swift* data with `xrtpipeline` along with the HEASARC remote CALDB[15] using the standard filtering procedure (Capalbi et al. 2005) to produce cleaned event files. We then further processed these files as described below. We also analyzed archival *Chandra* and *XMM-Newton* observations to have better spectral sensitivity at low energies ($\lesssim$3 keV). The *Chandra* data were reprocessed using `chandra_repro` of CIAO 4.4 along with CALDB 4.5.3, and the *XMM-Newton* data were processed with the Science Analysis System (SAS), version 12.0.1. See Figure 1 for *NuSTAR* images and Table 1 for a summary of the observations on which we report.

[15] See http://heasarc.nasa.gov/docs/heasarc/caldb/caldb_remote_access.html.

Table 1
Summary of Observations

Observatory	Obs. ID	Obs. Date (MJD)	Exposure (ks)	Mode[a]
Chandra[b]	730	51754	10.5	CC
XMM-Newton	0013340101	52552	3.9	FW/LW
XMM-Newton	0013340102	52554	4.4	FW/LW
Chandra[c]	6732	53946	24.9	TE
Swift	00080220003	56240	17.9	PC
NuSTAR	30001025002	56240	48.6	···

Notes.
[a] (PC) Photon counting; (TE) timed exposure; (FW) full window; (LW) large window; (CC) continuous clocking. MOS1,2/pn data are reported for *XMM-Newton*.
[b] Used only for 1E 1841−045.
[c] Used only for Kes 73, because of pileup.

3. DATA ANALYSIS AND RESULTS

3.1. Timing Analysis

We extracted source events in the 3–79 and 0.5–10 keV bands within circular regions of radius 60″ and 20″ for *NuSTAR* and *Swift*, respectively, and applied a barycentric correction to the event lists using the `barycorr` tool with the orbit files and the clock correction files using the position reported by Wachter et al. (2004). We then used the *H*-test (de Jager et al. 1989) to search for pulsations and to measure the period. Pulsations were detected with very high significance, and the best measured periods *P* were 11.79130(2) and 11.7914(2) s for *NuSTAR* and *Swift*, respectively. The uncertainties were estimated using the method given by Ransom et al. (2002). The periods we measured are consistent with those predicted on the basis of the ephemeris obtained with the *Swift* monitoring program, which will be described elsewhere (R. Archibald et al. 2013, in preparation).

Since we are measuring the properties of 1E 1841−045, the Kes 73 background must be subtracted; to do this optimally, the background region should be within the remnant, which extends out to 120″ in radius from the neutron star. Extracting backgrounds from a magnetar-free region within Kes 73 was straightforward in the *Swift* data, thanks to the XRT's good angular resolution; the backgrounds were extracted from an annular region with inner radius 60″ and outer radius 85″. However, extracting backgrounds was not easy for the *NuSTAR* data, since the point-spread function (PSF) is broad, and finding a source-free region within the remnant was not possible. Therefore, we extracted the background with inner and outer radii of 60″ and 100″ and then corrected for the source contamination in the background region (see Wang & Gotthelf 1998). The correction factor was calculated with *NuSTAR*'s measured instrumental PSF and estimated to be ∼10% (Harrison et al. 2013).

We also analyzed archival *Chandra* and *XMM-Newton* observations. For these data, source events were extracted from a

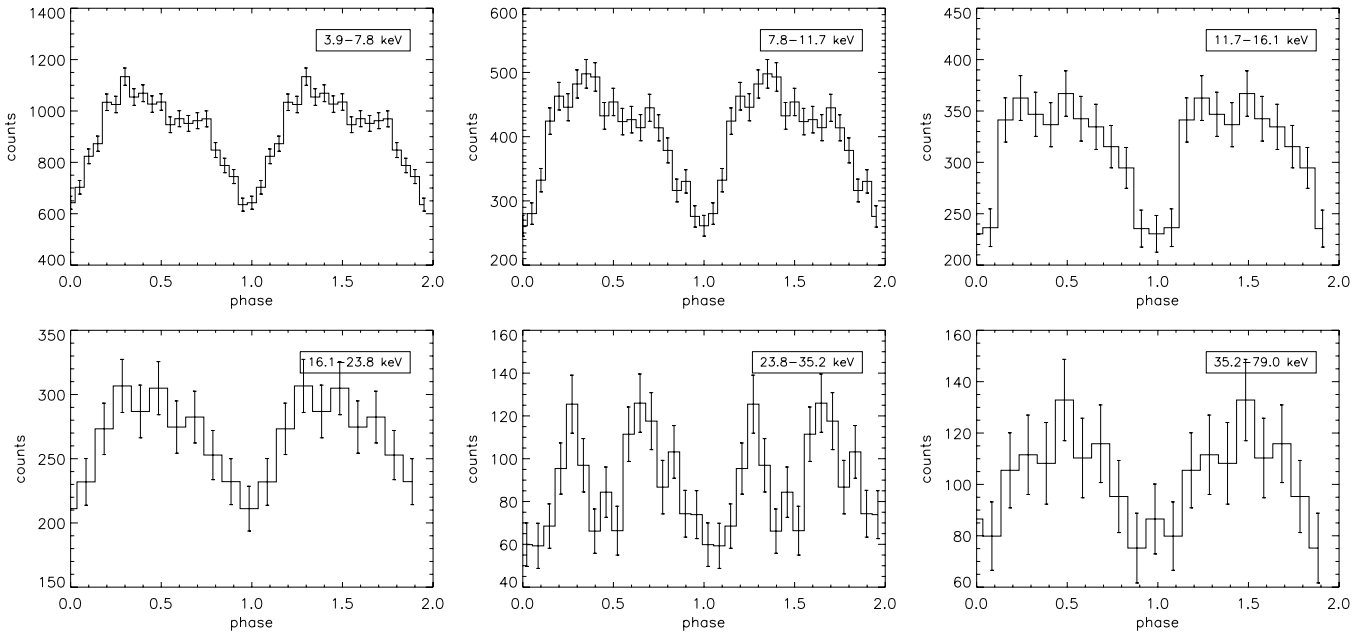

Figure 2. Pulse profiles for 1E 1841−045 from *NuSTAR* data in various energy bands. Note that the *y*-axis scales differ in the plots.

circle with radius 16″ and a ∼3″ × 10″ rectangle (continuous-clocking mode, 3″ along the event distribution), respectively. *XMM-Newton* backgrounds were extracted from events within an annulus with inner radius 48″ and outer radius 80″ centered at the source region, and *Chandra* backgrounds were extracted from two ∼5″ × 10″ rectangular regions offset 5″ to each side from the source. We then applied barycentric corrections to all the event lists for the temporal analysis below.

We folded the source-event time series at the best measured period to produce pulse profiles for multiple energy bands. The background level was subtracted from these pulse profiles. The background-subtracted pulse profiles obtained with *NuSTAR* are plotted in Figure 2. The energy bands were chosen to enable comparison with those reported by Kuiper et al. (2004). For each energy band, the significance of pulsation was greater than 99%.

The pulse profiles in Figure 2 qualitatively agree well with those reported by Kuiper et al. (2004). However, we see a double-peaked pulse profile in the 24–35 keV band. The profile in this band has not been previously reported. To see if the apparent double peak was a chance occurrence due to binning effects, we tried 250 different binnings by varying the zero phase. For each trial binning, we fitted the profile to two Gaussian functions and measured the significance of each peak. In all 250 cases, the significance was greater than 3 σ for both peaks. Moreover, the two peaks did not disappear when the energy range was adjusted slightly (e.g., 25–40 keV). Therefore, we conclude that they are genuine features in the light curve in this energy band.

In order to better constrain the transition energies of the feature, we produced pulsed profiles for smaller energy bins (2 keV). The double-peaked structure is visible to the eye from ∼26 to ∼34 keV, although the structure seen in these individual profiles may not be statistically significant.

We calculated the rms pulsed fraction, defined as

$$\mathrm{PF_{rms}} = \frac{\sqrt{2\sum_{k=1}^{4}\left(\left(a_k^2+b_k^2\right)-\left(\sigma_{a_k}^2+\sigma_{b_k}^2\right)\right)}}{a_0},$$

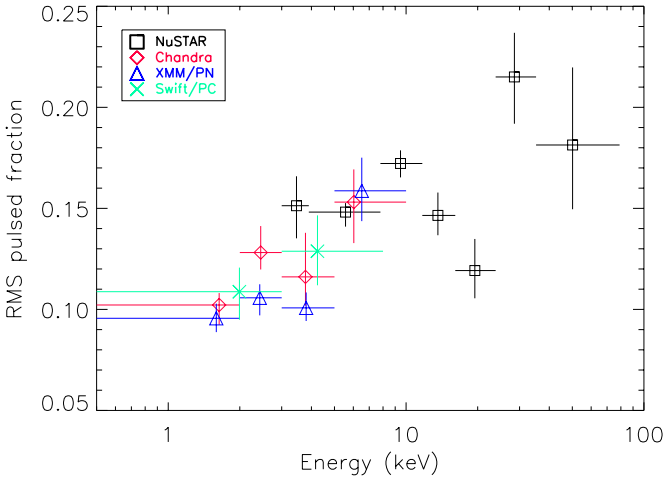

Figure 3. Pulsed fraction (rms) in several energy bands measured with the four X-ray telescopes. Note that the data point at ∼30 keV corresponds to the double-peaked structure in the pulse profile.

(A color version of this figure is available in the online journal.)

where $a_k = (1/N)\sum_{i=1}^{N} p_i \cos(2\pi ki/N)$, σ_{a_k} is the uncertainty in a_k, $b_k = (1/N)\sum_{i=1}^{N} p_i \sin(2\pi ki/N)$, σ_{b_k} is the uncertainty in b_k, p_i is the number of counts in the ith bin, N is the total number of bins, and n is the number of Fourier harmonics included, in this case $n = 4$ (see Gonzalez et al. 2010 for more details). We also performed similar analyses for the *XMM-Newton* and *Chandra* data, and the measured rms pulsed fractions are shown in Figure 3. We find that the rms pulsed fraction exhibits somewhat complicated behavior with energy; it is ∼20% around 50 keV but increases overall with energy.

We also searched for aperiodic variability with the *NuSTAR* data in the energy band from 3 to 79 keV. In particular, we searched for bursting activity in any energy band during the observations. We produced light curves with various time resolutions (0.1–1000 s) for several energy bands (e.g., 3–79, 15–79, 24–35 keV). We then searched for time bins having significantly larger than average numbers of events, accounting

Table 2
Phenomenological Spectral Fit Results for 1E 1841−045

Phase	Data[a]	Energy (keV)	Model[b]	N_H (10^{22} cm^{-2})	kT (keV)	Γ_s[c]	E_{break}/F_s[d] (keV)	Γ_h[e]	F_h[f]	L_{BB}[g]	χ^2/dof
0.0–1.0	S	0.5–10	BB+PL	2.23(25)	0.46(5)	1.76(39)	1.73(19)	···	···	1.58(29)	177/182
0.0–1.0	X, C	0.5–10	BB+PL	2.26(5)	0.42(1)	2.07(7)	1.74(5)	···	···	1.61(8)	1866/1849
0.0–1.0	N, S, X, C	0.5–79	BB+BP	2.24(4)	0.44(1)	2.09(4)	10.7(4)	1.33(3)	6.84(6)	1.91(8)	2440/2371
0.0–1.0	N, S, X, C	0.5–79	BB+2PL	2.58(10)	0.42(1)	2.96(18)	1.55(2)	1.06(9)	5.70(9)	1.24(21)	2427/2371
0.15–0.5	N, X, C	0.5–79	BB+BP	2.24[h]	0.44(1)	1.98(4)	12.4(9)	1.35(6)	7.50(7)	2.34(11)	819/797
0.5–0.8	N, X, C	0.5–79	BB+BP	2.24	0.44(1)	1.99(5)	12.6(8)	1.18(7)	7.78(9)	1.95(11)	687/652
0.8–1.15	N, X, C	0.5–79	BB+BP	2.24	0.45(1)	2.15(6)	10.0(5)	1.27(5)	5.79(7)	1.69(13)	606/633
0.15–0.5	N, X, C	0.5–79	BB+2PL	2.58	0.42(2)	2.99(13)	1.68(4)	1.19(10)	5.87(14)	1.51(26)	816/797
0.5–0.8	N, X, C	0.5–79	BB+2PL	2.58	0.45(4)	3.04(11)	1.51(4)	1.05(9)	6.45(16)	0.86(23)	680/652
0.8–1.15	N, X, C	0.5–79	BB+2PL	2.58	0.44(2)	2.91(11)	1.37(4)	0.91(11)	4.89(14)	1.33(22)	607/633
Pulsed[i]	X, C	0.5–10	PL	2.24	···	···	···	2.40(15)	0.43(4)	···	172/299
Pulsed	N, X, C	0.5–79	PL	2.24	···	···	···	1.98(7)	1.31(6)	···	429/640
Pulsed	N	5–79	PL	2.24	···	···	···	1.70(12)	1.58(15)	···	163/238
Pulsed	N	10–79	PL	2.24	···	···	···	1.36(23)	1.72(22)	···	79/114
Pulsed	N	15–79	PL	2.24	···	···	···	0.99(36)	1.76(27)	···	45/64

Notes. Uncertainties are at the 1 σ confidence level. When combining data from different observatories, cross-normalization factors were used. These were set to 0.9 for module A of *NuSTAR* (see Section 3.2), or 1 for *XMM-Newton* if *NuSTAR* data were not included. Fluxes were absorption-corrected and measured using the `cflux` model in XSPEC.

[a] (N) *NuSTAR*; (S) *Swift*; (X) *XMM-Newton*; (C) *Chandra*.

[b] (BB) Blackbody; (PL) power law; (BP) broken power law.

[c] Photon index for the soft power law component.

[d] Break energy for the broken power law (BB+BP) fit or soft power law flux (BB+2PL) in the 3–79 keV band if *NuSTAR* data were included. Otherwise, power-law flux in the 2–10 keV band is listed, in units of 10^{-11} erg cm^{-2} s^{-1}.

[e] Photon index for the hard power law component.

[f] Flux in units of 10^{-11} erg cm^{-2} s^{-1}. The values are only the (hard) power-law flux in the 3–79 keV band for the BP (PL, 2PL) model when the *NuSTAR* data are included; otherwise, power-law flux in the 2–10 keV band is listed.

[g] Blackbody luminosity in units of 10^{35} erg s^{-1} for an assumed distance of 8.5 kpc.

[h] N_H for the phase-resolved and pulsed spectral analysis was frozen.

[i] The `lstat` method in XSPEC was used for fitting pulsed spectra, and we report L-statistic/dof instead of χ^2/dof.

for the number of trials, but found none. Therefore, we conclude that there was no bursting activity on timescales of 0.1–1000 s during the observations.

3.2. Phase-averaged Spectral Analysis

We extracted the source and background events using the same regions defined in Section 3.1. To see if the *Swift* observation was piled up, we measured the count rate within a circle of radius 20 pixels (∼47″).[19] The count rate was ∼0.4 s^{-1}. Although the count rate was not high enough to produce pileup, we verified by removing the bright core (2″–4″ in radius) and found that there was no significant spectral change and thus no pileup. We also analyzed archival *Chandra* and *XMM-Newton* observations to see whether there is long-term spectral variability in the soft band and to combine with the *NuSTAR* observation, to have better spectral sensitivity in the soft band.

We first fitted the *Swift* data alone to see if there was any spectral change in the soft band (0.5–10 keV), since the last *Chandra* or *XMM-Newton* measurements were made ∼12 yr ago (e.g., Morii et al. 2003). We grouped the spectrum to have at least 20 counts per bin for the fit. We first fitted the data with an absorbed blackbody plus power law to compare with the archival *XMM-Newton* and *Chandra* data. The spectrum is a little harder than, but consistent with, previous results (Morii et al. 2003), as well as with our reanalysis of *XMM-Newton* plus *Chandra* data (see Table 2). We also tried to fit the *Swift* data with the same model using the best-fit parameters obtained from modeling of the *XMM-Newton* and *Chandra* data and found that the *Swift* spectrum is consistent with the model. Therefore, all four observations can be combined with the *NuSTAR* observation, and we report fit results for the combined data. Note that for the blackbody luminosities reported in Table 2, we assumed a distance of 8.5 kpc based on the H I absorption measurements of Tian & Leahy (2008).

We then tied all the model parameters between *NuSTAR*, *Swift*, *XMM-Newton*, and *Chandra* except for the cross-normalization factors (set to 0.9 for *NuSTAR*; the PSF correction factor) to fit the broadband spectrum (0.5–79 keV). To fit the data, we grouped the spectra to have at least 100 and 20 counts per bin for *NuSTAR* and the soft-band instruments (*Swift*, *XMM-Newton*, and *Chandra*), respectively. We tried to fit the data simultaneously with a blackbody plus power law. In the fitting, we used the 0.5–10 and 3–79 keV data for the soft-band instruments and for *NuSTAR*, respectively. The model was unacceptable, with χ^2 per degrees of freedom (dof) of 2634/2373, and adding one more component improved the fit significantly. Therefore, we fitted the data to an absorbed blackbody plus broken power law, `tbabs*(bbody+bknpow)`, or an absorbed blackbody plus two power laws, `tbabs*(bbody+pow+pow)` in XSPEC 12.7.1. The former is to be compared with the results of Kuiper et al. (2006) and the latter with those of Morii et al. (2010). We note that the blackbody component was required in both models. We show the spectra in Figure 4 and summarize the results in Table 2.

We studied the effects of nonuniformity in the Kes 73 SNR background, because the fit results may change depending on

[19] See http://www.swift.ac.uk/analysis/xrt/pileup.php.

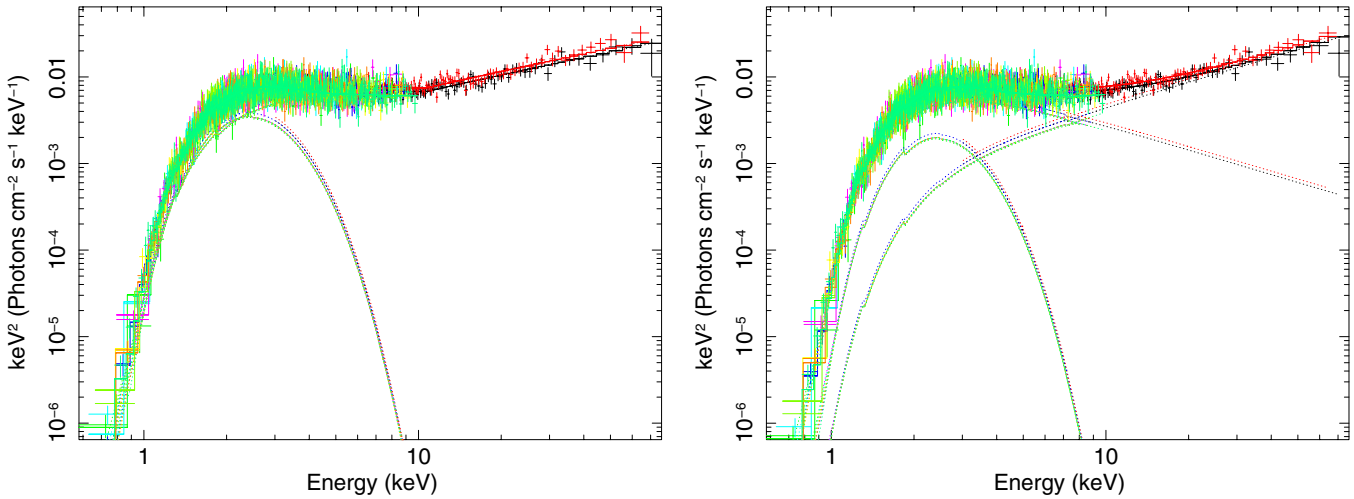

Figure 4. Phase-averaged spectra of *NuSTAR*, *Swift*, *XMM-Newton*, and *Chandra* data. Best-fit models and additive model components are also shown. Left: blackbody plus broken power law. Right: blackbody plus double power law.

(A color version of this figure is available in the online journal.)

the background region used. For *NuSTAR*, which operates in the 3–79 keV band with a relatively broad PSF, the effects of the thermal SNR and its spatial variation are likely to be very small. For other soft-band observatories, we first estimated the background to source count rates to be ∼15%, 6%, and 5% for the *Swift*, *XMM-Newton*, and *Chandra* data, respectively. Although variations on small background levels would not affect the spectral fit results much, the background level in the *Swift* data was relatively high, which may be a concern. Therefore, we used various background regions in the SNR for the spectral fits to the *Swift* and *XMM-Newton* data. As expected from the count-rate estimates, the *Swift* results fluctuated slightly (∼20%–40% of the statistical uncertainties) depending on the background region used, but the *XMM-Newton* results were more stable (∼6%–20% of the statistical uncertainties). We then used the various *Swift* and *XMM-Newton* backgrounds for the joint fit of the *NuSTAR*, *Swift*, *XMM-Newton*, and *Chandra* data and found that the spectral variations caused by different backgrounds were typically $\lesssim$10% of the statistical uncertainties.

We find that our best-fit parameters for the absorbed blackbody plus two power law model do not agree with those of Morii et al. (2010). We checked whether their spectral model is consistent with the *NuSTAR*, *Swift*, *XMM-Newton*, and *Chandra* data. We found that Morii et al.'s best-fit parameters do not describe our data. The null-hypothesis probability was 7×10^{-4} (χ^2/dof = 2601/2375), with a clear trend in the residuals at high energies ($\gtrsim$15 keV). We then varied their best-fit parameters for the absorbed blackbody plus two power law model ($N_{\rm H}$ = 2.836–2.896 $\times$ 10^{22} cm^{-2}, kT = 0.496–0.576 keV, $\Gamma_{\rm s}$ = 4.39–5.59, $\Gamma_{\rm h}$ = 1.42–1.82) within the uncertainties (defined as the direct sum of the statistical and systematic uncertainties, to maximize the parameter space) using the `steppar` command in XSPEC to see if we could find a set of parameters that is consistent with the data. The minimum χ^2/dof was 2530/2375, implying a null-hypothesis probability of ∼0.01, and some of the best-fit parameters hit the limit, reducing the probability. We then limited the fit to the 0.5–60 keV range similar to the *Suzaku* data and still found that the Morii et al. (2010) best-fit parameters were inconsistent with our data. We therefore conclude that the X-ray spectrum of 1E 1841−045 we measured cannot be explained with the spectral model reported by Morii et al. (2010).

3.3. Phase-resolved and Pulsed Spectral Analyses

We conducted a phase-resolved spectral analysis for three phase intervals, 0.15–0.5, 0.5–0.8, and 0.8–1.15, to catch distinct features in the pulse profiles (see Figure 2). The temporal resolutions of the *Swift* XRT and *XMM-Newton* Metal Oxide Semi-conductor (MOS) CCD arrays are comparable to the phase intervals we use here, and spectral mixing between different phases will occur, blurring the spectral differences among the phase intervals. Therefore, we ignored the *Swift* and *XMM-Newton* MOS data for the phase-resolved and pulsed spectral analysis below.

We binned the *NuSTAR* and the soft-band instruments' spectra to have at least 50 and 20 counts per spectral bin, respectively, and froze the cross normalizations to those obtained with the phase-averaged spectral fit. We fitted the spectra with two models: an absorbed blackbody plus broken power law, and an absorbed blackbody plus double power law. We find that the spectra vary with spin phase, and the detailed variation depends on the spectral model used. We report the results in Table 2.

We also fitted the pulsed spectrum after subtracting the unpulsed spectrum extracted in the phase interval 0.9–1.1. The *Chandra* and the *XMM-Newton* pn CCD data were phase-aligned with the *NuSTAR* data by correlating the light curves. Since the number of pulsed source counts per spectral bin was small, we used `lstat` because the usual χ^2 method may bias the results. We then froze the cross normalizations between instruments to the values obtained with the phase-averaged spectral fits.

There are not many events in the pulsed spectra, and a simple power-law model cannot be ruled out. However, we see rising trends in the residuals in the soft band ($\lesssim$2 keV) and hard band ($\gtrsim$10 keV). Also motivated by the very hard power-law component ($\Gamma \sim 0.7$) in the pulsed spectrum in the high-energy band (∼15–200 keV) reported by Kuiper et al. (2006), we gradually removed the soft bands from the spectral fit to see if the spectrum becomes very hard above ∼15 keV and found that indeed it does. We also tried to fit the data using alternative statistical methods (e.g., the usual χ^2 method or `cstat` in XSPEC) and found that the alternative methods gave similar results except for the fit in the 0.5–79 keV band, where

Table 3
Best-Fit Parameters of the Outflow Model

Solution	$\alpha_{\rm mag}$ (rad)	$\beta_{\rm obs}$ (rad)	θ_j (rad)	L[a]	μ[b]
1	0.3(2)	0.9(2)	<0.4	5(1)	>1.4
2	0.7(2)	1.4(1)	<0.4	5(1)	>1.4

Notes.
[a] Outflow power in units of $10^{36}(D/8.5\ {\rm kpc})^2$ erg s^{-1}.
[b] Magnetic dipole moment in units of 10^{32} G cm^3.

the χ^2 results were significantly different from the others. The results are summarized in Table 2.

We also measured spectral pulsed fractions in the hard band (defined as the ratio of pulsed and total spectra) in order to compare with those reported by Kuiper et al. (2006). We first fitted the total ($\gtrsim$11 keV) and the pulsed ($\gtrsim$15 keV) spectra to single-power-law models. The total spectrum above 11 keV is consistent with what we obtained using the absorbed blackbody plus broken power law (see Table 2). We then calculated the flux density ratio (which we refer to as the "spectral" pulsed fraction), finding it to be 24% ± 4% and 41% ± 18% at 20 and 80 keV, respectively. The uncertainties were estimated by simulating both pulsed and total spectra using the covariance matrices obtained during the spectral fitting. Using 10,000 simulations, we calculated the flux density ratios and the standard deviation to obtain the uncertainties.

Finally, we investigated the spectral properties of the double-peaked pulse profile in the 24–35 keV band (see Figure 2). With the double-peaked structure decidedly significant (see Section 3.1), we searched for evidence for this structure in the spectra. We detect a possible excess of counts at ∼30 keV in the spectrum in the phase bin 0.525–0.725 and a deficit at 0.325–0.525, but not in the spectra of the other phases. However, the continuum model alone is statistically acceptable, and the existence of an emission- or absorption-like feature cannot be clearly demonstrated with the present data.

3.4. Spectral Fits with the $e^{\pm}$ Outflow Model

Next we tested a new model proposed by Beloborodov (2013) to explain the hard X-ray emission from magnetars. The model envisions an outflow of relativistic electron–positron pairs created by pair discharge near the neutron star. The outflow moves along the magnetic field lines and gradually decelerates as it (resonantly) scatters the thermal X-rays. Its Lorentz factor decreases proportionally to the local magnetic field B,

$$\gamma \approx 100\frac{B}{B_Q}, \quad (1)$$

where $B_Q = m_e^2c^3/\hbar e = 4.44\times10^{13}$ G. This deceleration determines the emitted spectrum of resonantly scattered photons. The outflow fills the active "j-bundle" (an extended bundle of electric currents) of closed magnetospheric field lines (Beloborodov 2009). It radiates most of its kinetic energy in hard X-rays before the $e^{\pm}$ pairs reach the top of the magnetic loop and annihilate.

In a simple geometry, the j-bundle is axisymmetric and emerges from the polar cap around the magnetic dipole axis of the star. In this case, the model has the following parameters: (1) the angular size θ_j of the polar cap, (2) the power L of the $e^{\pm}$ outflow along the j-bundle, (3) the magnetic dipole moment μ of the star, (4) the angle $\alpha_{\rm mag}$ between the rotation axis and the magnetic axis, (5) the angle $\beta_{\rm obs}$ between the rotation axis and the observer's line of sight, and (6) the reference point of the rotational phase, ϕ_0. See Beloborodov (2013) for more details.

To test the model against data, we designed the following two-step method (R. Hascoët et al. 2013, in preparation): first, we explore the entire parameter space by fitting the phase-averaged total (pulsed + unpulsed) spectrum and the phase-resolved pulsed spectra. In this step, we only consider data above 10 keV, where the outflow dominates the observed radiation. For 1E 1841−045, we used three phase bins for the phase-resolved spectra (Section 3.3). We found that the model successfully fits the data, with the best-fit χ^2/dof = 1.13 (for 267 dof); the obtained parameters of the model are given in Table 3. For the best-fit model, the spectrum (νF_ν) peaks at ∼7 MeV. We also found a marginally acceptable (3σ confidence) second minimum (χ^2/dof = 1.22 for 267 dof). Both acceptable regions are well localized in the parameter space, and we show both solutions in Table 3.

In the second step, we freeze the best-fit parameters of the outflow model and fit the spectrum in the 0.5–79 keV band, using the *NuSTAR*, *Swift*, *Chandra*, and *XMM-Newton* data. This allows us to analyze possible models for the soft X-ray component. We found that the data exclude the single-blackbody model. On the other hand, the data are well fitted by a blackbody plus a power law or by a two-blackbody model. The results are summarized in Table 4. Note that the outflow model spectrum extends down to low energies, and thus the soft-band spectral parameters are different from those obtained using the phenomenological models (see Table 2).

4. DISCUSSION

We have reported on X-ray observations of the magnetar 1E 1841−045, most notably on its high-energy X-ray properties as observed by *NuSTAR*. We find that the pulse profile in the ∼24–35 keV band shows a double-peaked structure, which has not previously been reported. We also find that the rms pulsed

Table 4
Spectral Fit Results for the Soft Component of 1E 1841−045 from the Outflow Model

Model[a]	$N_{\rm H}$ (10^{22} cm^{-2})	kT_1 (keV)	kT_2 (keV)	Γ[b]	F[c]	$L_{\rm BB,1}$[d]	$L_{\rm BB,2}$[d]	χ^2/dof
BB+PL	2.90(8)	0.55(2)	···	3.79(11)	0.55(4)	1.08(10)	···	2316/2272
BB+BB	2.03(4)	0.45(1)	0.90(4)	···	···	2.15(7)	0.65(9)	2298/2272
BB	1.72(2)	0.57(1)	···	···	···	2.15(4)	···	2556/2274

Notes.
[a] (BB) Blackbody; (PL) power law.
[b] Photon index for the power-law component.
[c] Absorption-corrected flux of the power law in units of 10^{-11} erg cm^{-2} s^{-1} in the 3–79 keV band.
[d] Blackbody luminosity in units of 10^{35} erg s^{-1} for an assumed distance of 8.5 kpc.

fraction of the source is ∼20% at ∼50 keV. We show that the phase-averaged total spectrum of 1E 1841−045 can be modeled with an absorbed blackbody plus a broken power law or an absorbed blackbody plus two power laws. Finally, we constrained the geometry of the source by fitting the phase-averaged and the phase-resolved spectra with the electron–positron outflow model of Beloborodov (2013).

4.1. Pulse Profile

The pulse profiles measured with *NuSTAR* broadly agree with those previously measured with *RXTE* (Kuiper et al. 2004). However, we note some differences. In the 7.8–11.7 keV band, the previously measured profile had a flat top, from which Kuiper et al. (2004) suggested that the dominance of the two pulses (one at phase ∼0.3 and the other at ∼0.7) changes at ∼9 keV. In the *NuSTAR* observation, the flattening occurred at 11.7–16.1 keV, implying the change is at ∼11 keV, similar to the location of the spectral break (see Table 2). Temporally measuring the exact energy over which the flattening occurs was difficult, and the difference between ∼9 and ∼11 keV may be marginal.

We found a double-peaked structure in the ∼24–35 keV band. It is not unusual for a magnetar's pulse profiles to change with energy. For example, den Hartog et al. (2008a, 2008b) showed that the pulse profiles of two magnetars, AXP 1RXS J170849−400910 and AXP 4U 0142+61, change with energy. Furthermore, the two magnetars have separate peaks in their pulse profiles that correspond to the soft- and hard-band emission, respectively. It seems that the soft emission peak leads the hard one in phase at least for those two magnetars (when considering the pulse minimum as phase zero). Although we could not clearly identify a hard peak at higher energies for 1E 1841−045, the peak at phase ∼0.6 in the 24–35 keV band may be its counterpart; our phase-resolved spectral analysis suggests this (see Table 2). If this is correct, 1E 1841−045 behaves similarly to AXP 1RXS J170849−400910 and AXP 4U 0142+61; the soft emission peak leads the hard one (see also Göğüş et al. 2010, for SGR 0501+4516). It will be interesting to see if this trend is common to other magnetars.

The pulsed fraction of the source is known to increase with energy (Kuiper et al. 2006; Morii et al. 2010), and we confirm this (see Figure 3). Furthermore, Kuiper et al. (2006) reported that the pulsed fraction of 1E 1841−045 is ∼25% at 20 keV and ∼100% above ∼100 keV. Note that our measured rms pulsed fractions shown in Figure 3 cannot be directly compared with those reported by Kuiper et al. (2006), because they reported a spectral pulsed fraction. Therefore, we calculated the spectral pulsed fraction (Section 3.3) for comparison. We found that the spectral pulsed fractions are 24%±4% at 20 keV and 41%±18% at 80 keV. While these values may be consistent with those of Kuiper et al. (2006), they may agree better with a reanalysis of the *RXTE* and *INTEGRAL* data including more exposure (L. Kuiper et al. 2013, in preparation).

4.2. Spectrum

We found that the spectral parameters of Morii et al. (2010) are inconsistent with those we obtained using *NuSTAR*, *Swift*, *XMM-Newton*, and *Chandra* data. It is possible that the discrepancy between our results and those found using *Suzaku* is due to spectral variability in the source. However, the source is known to be fairly stable, at least in the soft band (Zhu et al. 2010; Lin et al. 2011; Dib & Kaspi 2013). Morii et al. (2010) noted that the PSF of *Suzaku* is broad (half-power diameter HPD = 2′), and it was difficult to subtract the Kes 73 background. Indeed, they used an SNR model obtained with *Chandra* to estimate the Kes 73 background instead of directly subtracting a measured background. This may pose a problem in the soft band, because the *Chandra* SNR model fit was not very good, as previously noted by Zhu et al. (2010); residuals in the Kes 73 model fit would be attributed to the 1E 1841−045 spectrum. We independently checked whether the Kes 73 model (`vsedov`) used by Morii et al. (2010) fitted the *Chandra* and *XMM-Newton* data well and found that reduced χ^2 values for the model were ∼1.3–2.3, leaving significant residuals after the fit. Moreover, the number of SNR background events is estimated to be ∼70% larger than that of the source events for a circle of radius 110″ in the *XMM-Newton* data. Therefore, any residuals in the Kes 73 model fits will be amplified unless the source extraction region is small, which Morii et al. (2010) could not do because of the large HPD of *Suzaku*. Furthermore, difficulty in subtracting the high-energy background (e.g., Galactic ridge emission and cosmic X-ray background) in the data from the *Suzaku* Hard X-Ray Detector could have made their analysis inaccurate.

Morii et al. (2010) argued that the residuals are present only at the Kes 73 emission lines and did not affect the continuum model of the point source. It is not clear whether the residuals are really only at the emission lines (see, e.g., their Figure 2), and even if so, it is not clear that they do not affect the results for such a complicated point-source spectral model.

Both BB+BP and BB+2PL models are phenomenological, and we use them mainly for comparison with previous data analyses. Although both provide a good fit to our data, a BB+BP model is more consistent with the observations above 80 keV by Kuiper et al. (2006). Note that our analysis results support the anticorrelation between $\Gamma_s - \Gamma_h$ and B reported by Kaspi & Boydstun (2010), and a correlation between hardness ratio (F_h/F_s, ratio of hard to soft spectral component flux in the 1–60 keV band) and the characteristic age inferred from the spin-down rate by Enoto et al. (2010).

We note that the soft-band spectrum measured with *Swift* in 2012 November is consistent with those measured by *XMM-Newton* and *Chandra* 12 yr ago. It has been suggested that the soft-band spectrum of the source has been stable over 13 yr between 1993 and 2007 (Zhu et al. 2010). This is despite numerous spin-up glitches and bursts (Dib et al. 2008; Lin et al. 2011). Our observations support this, in agreement with the results of Dib & Kaspi (2013), which were based only on the pulsed flux.

We found a hint of a spectral excess at ∼30 keV in the phase interval that corresponds to the pulse peak (phase ∼0.6) of the 24–35 keV pulse profile (see Figure 2). A hint of a spectral deficit was also found at the same energy, but in a different phase interval (phase ∼0.45). If we interpret this as a cyclotron line feature, the inferred magnetic field strength would be $\sim 3\times10^{12}$ G for electrons, or $\sim 5\times10^{15}$ G for protons. The magnetic field strength for the electron cyclotron line is similar to those in the zone where the outflowing plasma radiates all its energy (Beloborodov 2013). Although the excess and deficit might be produced by line emission, longer observations are required in order to demonstrate this.

With our 48 ks *NuSTAR* observation, the measurement of the pulsed spectrum in the hard X-ray band is not very precise. The obtained spectral slope in the 15–79 keV range is $\Gamma = 0.99 \pm 0.36$. This is consistent with the $\Gamma = 0.72 \pm 0.15$ observed by *RXTE* and *INTEGRAL* in the 15–200 keV range

(Kuiper et al. 2006). Morii et al. (2010) reported a different index for the pulsed spectrum, $\Gamma = 2.45^{+0.20}_{-0.21}$. Note, however, that they used a different energy band, 0.7–25 keV, heavily weighted in the soft band (<10 keV) and thus more representative of the soft-band spectrum. When we limit our analysis to the 0.5–25 keV band with an $N_{\rm H}$ of 2.87×10^{22} cm^{-2} (similar to those of Morii et al. 2010), we find $\Gamma = 2.19 \pm 0.09$, consistent with Morii et al. (2010). Although we argued above that the *Suzaku* spectral results might have been biased by contamination from Kes 73, the situation for the pulsed spectrum is different, because the Kes 73 spectrum is subtracted in a model-independent way when subtracting the DC component. Therefore, the agreement with *Suzaku* results for the pulsed spectrum is unsurprising.

When limiting the analysis to the 2–25 keV band with $N_{\rm H} = 2.54 \times 10^{22}$ cm^{-2} (similar to those used by Kuiper et al. 2004), the photon index became 2.00 ± 0.08, consistent with 1.98 ± 0.02, the value reported by Kuiper et al. (2004).

4.3. Outflow Model

We found that the phase-resolved spectrum of 1E 1841−045 is consistent with the model of Beloborodov (2013). In this model, the X-ray emission comes from the active *j*-bundle filled with a relativistic $e^{\pm}$ outflow, whose Lorentz factor decreases according to Equation (1). The best-fit physical parameters are in agreement with theoretical expectations. Specifically, the active *j*-bundle is constrained to emerge from a polar cap of angular size $\theta_j \approx 0.4$ rad, and the outflow power is measured to be $L \approx 5 \times 10^{36} (D/8.5\ {\rm kpc})^2$ erg s^{-1}. Using Equation (48) of Beloborodov (2009), one can estimate the voltage of $e^{\pm}$ discharge in the magnetosphere of 1E 1841−045. This gives $\Phi \approx 10^{10} \psi^{-1}$V, where $\psi \sim 1$ rad is the magnetic twist implanted in the *j*-bundle and we have used a magnetic moment for the neutron star of $\mu \approx 7 \times 10^{32}$ G cm^3, which was estimated from the spin-down rate (Dib et al. 2008). The obtained voltage is in the expected range of 10^9–10^{10}V (Beloborodov & Thompson 2007).

The outflow power L must be equal to the bolometric luminosity emitted in hard X-rays. The best-fit model shows that the spectrum peaks at ∼7 MeV, outside the *NuSTAR* energy range. The exact location of the peak changes depending on the solution (Table 3) but is still in the MeV band. This is consistent with previous observations by *INTEGRAL* and *RXTE* (Kuiper et al. 2006). Our analysis also gives constraints on the geometry of the magnetized rotator in 1E 1841−045 (see Table 3), which may be tested and refined by future measurements of X-ray polarization (or radio polarization, if the source one day becomes radio-bright), or by incorporating future modeling of the pulse profile.

We find that the hard X-ray emission from the $e^{\pm}$ outflow extends below 10 keV and must be included in the analysis of the soft X-ray component. When this contribution is taken into account, we find that (1) a single blackbody does not provide a good fit for the soft X-ray emission, (2) a two-temperature blackbody provides the best fit, and (3) a good fit is also provided by a blackbody plus a power law (Table 4).

The two-temperature blackbody model admits a simple physical interpretation. The cold blackbody, $kT_1 \approx 0.45$ keV, corresponds to the main thermal emission of the neutron star, and the hot blackbody, $kT_2 \approx 0.9$ keV, comes from a hot spot. The inferred emission areas of the cold and hot blackbodies are $\mathcal{A}_1 \sim \mathcal{A}_{\rm NS}/2$ and $\mathcal{A}_2 \sim 10^{-2} \mathcal{A}_{\rm NS}$, where $\mathcal{A}_{\rm NS}$ is the area of the neutron star surface (assuming a radius $R_{\rm NS} = 10$ km). Interestingly, $\mathcal{A}_2$ is comparable to the area of the *j*-bundle footprint, $\mathcal{A}_j \approx \pi \sin^2 \theta_j R_{\rm NS}^2$. The footprint is expected to be hotter than the rest of the stellar surface, as it can be bombarded by the particles flowing in the *j*-bundle toward the neutron star. Similar hot spots have been reported in some other magnetars (e.g., Gotthelf & Halpern 2007; Tiengo et al. 2008).

The soft X-ray component could also be modeled as a single blackbody modified by resonant scattering in the magnetosphere (Thompson et al. 2002). Such a modification may be expected from scattering by the decelerated, mildly relativistic $e^{\pm}$ pairs in the equatorial region of magnetosphere (Beloborodov 2013). This effect is, however, currently difficult to model, because it is sensitive to the poorly understood velocity distribution of the highly opaque $e^{\pm}$ plasma near the magnetic equatorial plane.

5. CONCLUSIONS

We have analyzed 48 ks *NuSTAR* and simultaneous 18 ks *Swift* observations, and archival data from *XMM-Newton* and *Chandra*, for the magnetar 1E 1841−045. To compare with previous observations, we fitted the source spectra with two phenomenological models: an absorbed blackbody plus broken power law, and an absorbed blackbody plus two power laws. The measured spectral parameters are consistent with those reported by Kuiper et al. (2006), and the photon index in the hard X-ray band is better constrained with the *NuSTAR* data than before. However, the *NuSTAR* data are not consistent with the spectral parameters reported by Morii et al. (2010). Although it is possible that the source might have varied since the *Suzaku* observations, it seems likely that an imperfect Kes 73 model caused problems in the background subtraction of the *Suzaku* data.

Our measurements of the pulsed spectrum are less constraining than, but consistent with, those in Kuiper et al. (2006). The pulsed spectrum is also consistent with *Suzaku* observations. We measured the rms pulsed fraction to be ∼20% at ∼50 keV. Although the spectral pulsed fractions were not well constrained at high energies, our results suggest that the pulsed fraction is likely to be significantly lower than 100% at 100 keV.

We find that the pulse profile in the ∼24–35 keV band shows a double-peaked structure, which has not been reported previously. The deviation of the pulse profile localized in a narrow energy range suggests a possible absorption (or emission) feature in the phase-resolved spectrum. Although we find some evidence for such a feature, it is not statistically significant in the present data and requires deeper observations for possible confirmation.

The phase-resolved spectrum of 1E 1841−045 is consistent with the emission model of Beloborodov (2013). From the model fit, we obtain constraints on the angle between the rotation and magnetic axes of the neutron star. We also infer the size of the active *j*-bundle, the power of the $e^{\pm}$ flow, and the voltage of the $e^{\pm}$ discharge, all of which agree with theoretical expectations. The results imply that the spectrum peaks at ∼7 MeV. Using this model, we placed constraints on the geometric properties of the magnetar that, in principle, could be tested with future observations.

Using the physical model for the hard X-ray emission, we revisited the analysis of the soft X-ray component. We found that its phase-averaged spectrum can be fitted by two blackbodies and that the hot-blackbody area is consistent with that expected for the footprint of the active *j*-bundle. However, we cannot rule out a power law plus blackbody for the soft component; future, deeper observations may help in this regard.

This work was supported under NASA contract NNG08FD60C, and made use of data from the *NuSTAR* mission, a project led by the California Institute of Technology, managed by the Jet Propulsion Laboratory, and funded by the National Aeronautics and Space Administration. We thank the *NuSTAR* Operations, Software, and Calibration Teams for support with the execution and analysis of these observations. This research has made use of the *NuSTAR* Data Analysis Software (NuSTARDAS), jointly developed by the ASI Science Data Center (ASDC, Italy) and the California Institute of Technology (US). V.M.K. acknowledges support from an NSERC Discovery Grant, the FQRNT Centre de Recherche Astrophysique du Québec, an R. Howard Webster Foundation Fellowship from the Canadian Institute for Advanced Research (CIFAR), the Canada Research Chairs Program, and the Lorne Trottier Chair in Astrophysics and Cosmology. A.M.B. acknowledges the support by NASA grants NNX10AI72G and NNX13AI34G. Part of this work was performed under the auspices of the US Department of Energy by Lawrence Livermore National Laboratory under contract DE-AC52-07NA27344.

REFERENCES

Baring, M. G., & Harding, A. K. 2007, Ap&SS, 308, 109
Beloborodov, A. M. 2009, ApJ, 703, 1044
Beloborodov, A. M. 2013, ApJ, 762, 13
Beloborodov, A. M., & Thompson, C. 2007, ApJ, 657, 967
Capalbi, M., Perri, M., Saija, B., Tamburelli, F., & Angelini, L. 2005, The Swift XRT Data Reduction Guide, Technical Report 1.2, http://swift.gsfc.nasa.gov/analysis/xrt_swguide_v1_2.pdf
de Jager, O. C., Swanepoel, J. W. H., Raubenheimer, B. C., et al. 1989, A&A, 221, 180
den Hartog, P. R., Kuiper, L., & Hermsen, W. 2008a, A&A, 489, 263
den Hartog, P. R., Kuiper, L., Hermsen, W., et al. 2008b, A&A, 489, 245
Dib, R., & Kaspi, V. M. 2013, ApJ, submitted
Dib, R., Kaspi, V. M., & Gavriil, F. P. 2008, ApJ, 673, 1044
Duncan, R. C., & Thompson, C. 1992, ApJL, 392, L9
Enoto, T., Nakazawa, K., Makishima, K., et al. 2010, ApJL, 722, L162
Göğüş, E., Woods, P. M., Kouveliotou, C., et al. 2010, ApJ, 722, 899
Gonzalez, M. E., Dib, R., Kaspi, V. M., et al. 2010, ApJ, 716, 1345
Gotthelf, E. V., & Halpern, J. P. 2007, Ap&SS, 308, 79
Hailey, C. J., An, H., Blaedel, K. L., et al. 2010, Proc. SPIE, 7732, 77320T
Harrison, F. A., Cook, W. R., Miyasaka, H., & McLean, R. 2010, in Semiconductor Radiation Detection Systems (Boca Raton, FL: CRC Press), 67
Harrison, F. A., Craig, W. W., Christensen, F. E., et al. 2013, ApJ, 770, 103
Heyl, J. S., & Hernquist, L. 2005, ApJ, 618, 463
Kaspi, V. M., & Boydstun, K. 2010, ApJL, 710, L115
Kouveliotou, C., Dieters, S., Strohmayer, T., et al. 1998, Natur, 393, 235
Kuiper, L., Hermsen, W., den Hartog, P. R., & Collmar, W. 2006, ApJ, 645, 556
Kuiper, L., Hermsen, W., & Mendez, M. 2004, ApJ, 613, 1173
Lin, L., Kouveliotou, C., Göğüş, E., et al. 2011, ApJL, 740, L16
Livingstone, M. A., Scholz, P., Kaspi, V. M., Ng, C.-Y., & Gavrill, F. P. 2011, ApJL, 743, L38
Mereghetti, S. 2008, A&ARv, 15, 255
Molkov, S. V., Cherepashchuk, A. M., Lutovinov, A. A., et al. 2004, SvAL, 30, 534
Morii, M., Kitamoto, S., Shibazaki, N., et al. 2010, PASJ, 62, 1249
Morii, M., Sato, R., Kataoka, J., et al. 2003, PASJ, 55, L45
Olausen, S. A., & Kaspi, V. M. 2013, ApJ, submitted
Ransom, S. M., Eikenberry, S. S., & Middleditch, J. 2002, ApJ, 124, 1788
Rea, N., & Esposito, P. 2011, in High-Energy Emission from Pulsars and Their Systems, ed. D. F. Torres & N. Rea (Berlin: Springer), 247
Rea, N., Esposito, P., Turolla, R., et al. 2010, Sci, 330, 944
Rea, N., Israel, G. L., Esposito, P., et al. 2012, ApJ, 754, 27
Scholz, P., Ng, C. Y., Livingstone, M., et al. 2012, ApJ, 761, 66
Thompson, C., & Beloborodov, A. M. 2005, ApJ, 634, 565
Thompson, C., & Duncan, R. C. 1996, ApJ, 473, 322
Thompson, C., Lyutikov, M., & Kulkarni, S. R. 2002, ApJ, 574, 332
Tian, W. W., & Leahy, D. A. 2008, ApJ, 677, 292
Tiengo, A., Esposito, P., & Mereghetti, S. 2008, ApJL, 680, L133
Vasisht, G., & Gotthelf, E. V. 1997, ApJL, 486, L129
Wachter, S., Patel, S. K., Kouveliotou, C., et al. 2004, ApJ, 615, 887
Wang, Q. D., & Gotthelf, E. V. 1998, ApJ, 494, 623
Woods, P. M., & Thompson, C. 2006, in Compact Stellar X-ray Sources, ed. W. H. G. Lewin & M. van der Klis (Cambridge: Cambridge Univ. Press), 547
Zhu, W., & Kaspi, V. M. 2010, ApJ, 719, 351